Band structure and excitonic properties of WSe_2 in the isolated monolayer limit in an all-electron approach

Niloufar Dadkhah* and Walter R. L. Lambrecht†
Department of Physics, Case Western Reserve University, 10900 Euclid Avenue, Cleveland, Ohio 44106-7079

(Received 2 April 2024; accepted 30 April 2024; published 17 May 2024)

We present a study of the electronic band structure and optical absorption spectrum of monolayer WSe_2 using an all-electron quasiparticle self-consistent *GW* approach, QS$G\hat{W}$, in which the screened Coulomb interaction $\hat{W}$ is calculated including ladder diagrams representing the electron-hole interaction. The Bethe-Salpeter equation is used to calculate both the screened Coulomb interaction $\hat{W}$ in the quasiparticle band structure and the imaginary part of the macroscopic dielectric function. The convergence of the quasiparticle band gap and lowest exciton peak position is studied as a function of the separation of the monolayers when using periodic boundary conditions. The quasiparticle gap is found to vary as $1/d$ with d the size of the vacuum separation, while the lowest excitonic peak reaches convergence much faster. The nature of the exciton spectrum is analyzed and shows several peaks below the quasiparticle gap when a sufficient number of **k** points is used. The results are found to be in good agreement with previous theoretical and experimental studies after adding spin-orbit coupling corrections and can be explained in the context of the Wannier-Mott theory adapted to two dimensions.

DOI: 10.1103/PhysRevB.109.195155

I. INTRODUCTION

It is well known that two-dimensional (2D) materials show strong excitonic effects owing to reduced screening in two dimensions [1,2] and the intrinsic differences between the 2D and 3D Coulomb problem [3]. The lower dimensionality also has a strong effect on the quasiparticle self-energy [4–7]. Transition metal dichalcogenides are a well studied family of 2D materials which can be isolated in monolayer form. In practice, these monolayers are always placed on a substrate and often also capped with additional layers such as hexagonal boron nitride (hBN). This provides additional screening of the surroundings of the monolayer. Determining the true isolated monolayer properties of a freestanding layer experimentally is thus a challenging task. This was achieved for the optical gap in [8] but not for the quasiparticle gap. On the other hand, computationally, determining the isolated limit is also challenging because almost all calculations rely on periodic boundary conditions and thus the convergence as a function of interlayer spacing needs to be studied carefully. To overcome this, some methods use a truncation of the Coulomb interaction in the direction perpendicular to the layers [9–11] or a mixed space approach [12]. In this paper, we pick WSe_2 as an example to re-evaluate this question by extrapolating as a function of the inverse distance between the layers.

Many-body-perturbation theory (MBPT) currently provides the most accurate approach to the electronic band structure in the form of Hedin's *GW* approach [13,14] where G is the one-electron Green's function and W the screened Coulomb interaction. Likewise, the Bethe-Salpeter equation (BSE) approach [15–21] provides an accurate approach for optical absorption including local field and electron-hole interaction effects. Most of the implementations of these methods start from density functional theory (DFT) in the local density approximation (LDA) or the generalized gradient approximation (GGA) and make use of pseudopotentials and plane wave basis sets. Here we use an all-electron implementation based on the full-potential linearized muffin-tin orbital (FP-LMTO) method [22,23], which uses an auxiliary basis set consisting of interstitial plane waves and products of partial waves [24] inside spheres to represent two-point quantities, such as the bare and screened Coulomb potentials, v, W, the polarization propagator P and the inverse dielectric response function ε^{-1}.

Different levels of the *GW* approximation are in use. The most commonly used method is the G_0W_0 approximation, in which perturbation theory is used to find the correction due to the difference between the *GW* self-energy operator and the DFT exchange correlation potential used at zeroth order. Self-consistent *GW* in the sense conceived by Hedin [13] does not necessarily improve the results because it appears to require one to include vertex corrections and go beyond the *GW* approximation. A successful way to make the results of *GW* independent of the starting point is the quasiparticle self-consistent *GW* approach (QSGW) [22,25]. Nonetheless, this method overestimates the quasiparticle gaps because it underestimates screening. Typically, it underestimates dielectric constants of semiconductors by about 20% as illustrated for example in Fig. 1 in Ref. [26]. To overcome this problem, several approaches are possible. One can include electron-hole interactions in the screening of W by means of a time-dependent density functional approach by including a suitable exchange-correlation kernel [27,28]. The approach we use here was recently introduced by Cunningham *et al.*

*niloufar.dadkhah@case.edu
†walter.lambrecht@case.edu

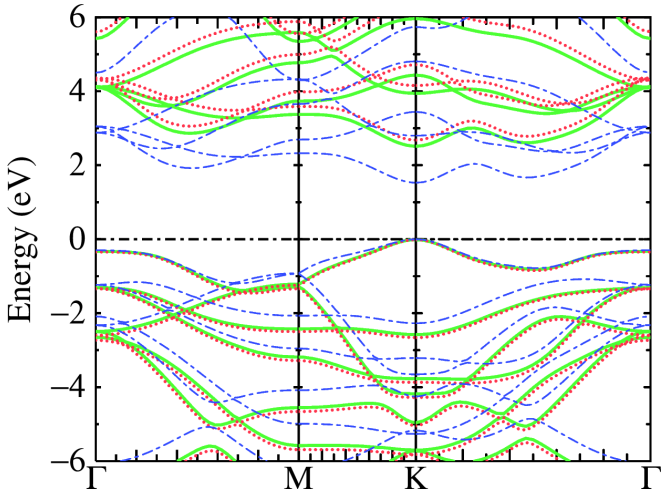

FIG. 1. Band structure of WSe_2 in the LDA (blue dashed dotted), QSGW (red dotted), and QS$G\hat{W}$ (green solid). The bands are referred to the valence band maximum within each method.

[29–31] and includes ladder diagrams in the screening of W via a BSE for $W(\mathbf{q}, \omega = 0)$. It can also be viewed as introducing a vertex correction in the Hedin's equation for W. No vertex corrections are included in the self-energy Σ, but this is justified within the QSGW approach by the approximate cancellation in the $\mathbf{q} \to 0$, $\omega \to 0$ limits of the Z factors in the vertex $\Gamma \propto 1/Z$ and the coherent part of the Green's function $G = ZG^0 + \tilde{G}$ [31]. Here $Z = (1 - \partial\Sigma/\partial\omega)^{-1}$ is the renormalization factor from the quasiparticlized G^0 to the dynamic G Green's functions and $\tilde{G}$ is the incoherent part of the Green's function.

Given this new methodological development, it is of interest to apply this approach to an already well-studied system, such as WSe_2, which is one of the main goals of this work. Other goals are to study the convergence of various aspects of the method, such as the number of bands included in the BSE approach, QSGW without and with ladder diagrams, which we call QS$G\hat{W}$, and how these affect the dependence of the gap on the size of the vacuum region. We compare our results with previous theory and experimental work and discuss the nature of the excitons. Our results confirm the main conclusion of Komsa *et al.* [6] in a study of MoS_2 that the long-range effects of the self-energy in GW lead to a slow $1/d$ convergence of the quasiparticle gap with d the size of the vacuum region but with a similar and compensating slow convergence of the exciton binding energy, resulting in a much faster convergence of the optical gap corresponding to the lowest allowed exciton peak. This same conclusion was also already obtained for hBN by Wirz *et al.* [7]. Beside the behavior as a function of distance, which we find to mainly affect the quasiparticle gap, we show that the convergence of the exciton energy as a function of the $\mathbf{k}$ mesh included in the BSE calculations is crucial to obtain good agreement with the exciton gap and is even more important to obtain an accurate representation of the spectrum of exciton states beyond the ground state exciton. We study the spectrum of exciton levels below the quasiparticle gap, including dark excitons and explain their localization in $\mathbf{k}$ space and real space in relation to the 2D Wannier-Mott theory. Spin-orbit coupling (SOC) effects are included in the bands and added as *a posteriori* corrections to the excitons. Our work on the exciton spectrum analysis is inspired by the approach of Qiu *et al.* [11] but, in spite of our more limited $\mathbf{k}$ mesh is able to resolve various aspects of the real-space and $\mathbf{k}$-space behavior of the Wannier-Mott theory envelope function of the excitons.

II. COMPUTATIONAL METHOD

The band structure calculations carried out here use the QUESTAAL package, which implements DFT and MBPT using a LMTO basis set [23]. The details of the QSGW approach and its justification compared to fully self-consistent GW in the Hedin set of equations, can be found in Ref. [22]. The recent implementation of the BSE in this code is documented in Refs. [29–31]. Briefly, in this approach the screened Coulomb interaction is calculated beyond the random phase approximation (RPA) by including ladder diagrams. Diagrammatically, this means opening the loop diagram $P^{\rm RPA}(12) = -iG(12)G(21) \equiv P^{\rm RPA}(1122)$ to a four-point polarization $P^{\rm RPA}$ and inserting the W electron-hole interactions via a Dyson-type equation and then recontracting to a two-point polarization,

$$P(12) = P^{\rm RPA}(12) - \int d(34) P^{\rm RPA}(1134) W(34) P(3422) \tag{1}$$

with $P^{\rm RPA}(1234) = -iG(13)G(42)$. While here, the numbers $1-4$ stand for particle position, spin and time, this is done in practice by Fourier transforming to the frequency domain and expanding in products of one-particle eigenfunctions. At this point, we make the approximation of using only the static $W(\mathbf{q}, \omega = 0)$ in the above Eq. (1), but keeping the frequency dependence in the P inherited from its $P^{\rm RPA}(\mathbf{q}, \omega)$. Furthermore we make the Tamm-Dancoff approximation so that the inversion of the above integral equation boils down to diagonalizing an effective Hermitian two-particle Hamiltonian with the W kernel,

$$H^{(2p)}_{vc\mathbf{k}v'c'\mathbf{k}'}(\mathbf{q}) = (\epsilon_{c\mathbf{k}+\mathbf{q}} - \epsilon_{v\mathbf{k}})\delta_{vv'}\delta_{cc'}\delta_{\mathbf{k}\mathbf{k}'} - (f_{c\mathbf{k}+\mathbf{q}} - f_{v\mathbf{k}}) W_{vc\mathbf{k}v'c'\mathbf{k}'}(\mathbf{q}), \tag{2}$$

where $\epsilon_{n\mathbf{k}}$ are the one particle eigenvalues and $f_{n\mathbf{k}}$ are Fermi occupation functions. We then obtaining the spectral representation,

$$P_{vc\mathbf{k}v'c'\mathbf{k}'}(\mathbf{q}, \omega) = [H^{(2p)}(\mathbf{q}) - \omega]^{-1}_{vc\mathbf{k}v'c'\mathbf{k}'}(f_{c'\mathbf{k}'+\mathbf{q}} - f_{v'\mathbf{k}'}), \tag{3}$$

which is then contracted to its two point form and inserted in the usual equation for $W = [1 - vP]^{-1}v$ to find the updated W with ladder diagrams, called $\hat{W}$. Thus, while the static approximation $\omega = 0$ for W is used to facilitate the solution of the equation to obtain an improved polarization propagator P beyond the RPA, the frequency dependence of P and hence the final W is maintained. However, contrary to the usual BSE approach for the macroscopic dielectric function which only involves the $\mathbf{q} \to 0$ limit, here we need to diagonalize a two particle Hamiltonian at each $\mathbf{q}$ point used in the evaluation of the GW self-energy. Finally for the macroscopic dielectric function calculations, a similar BSE equation approach is used

but now with the usual kernel $\bar{V} - W$ where the $\bar{V}$, the microscopic bare Coulomb interaction term incorporates the local field effects and W incorporates the electron-hole interactions. This is only a brief overview of the approach which is fully discussed in Ref. [30].

In the following, we summarize our convergence parameters for their application to WSe_2. We use a double (κ, R_{sm}) basis set *spdfgspdf* on W, with $5p$ semicore states and $6d$ high-lying states treated as local orbitals. Here κ^2 is the Hankel function kinetic energy and R_{sm} is the smoothing radius of the smoothed Hankel function envelope function. For Se, we use a *spdfspd* basis set. The quasiparticle self-energy matrix is calculated up to a cutoff of 2.5 Ry and is approximated by an average diagonal value above 2.0 Ry. Convergence is studied as a function of the **k** mesh on which the self-energy is calculated and subsequently interpolated to a finer mesh or along the symmetry lines by Fourier transforming back and forth to the real space LMTO basis set. We find that a $9 \times 9 \times 3$ set is converged to within 0.1 eV. Somewhat surprisingly, even for a vacuum region as large as 35 Å, we need more than one **k** division in the short direction of the reciprocal unit cell perpendicular to the layers in order to obtain a clear $1/d$ behavior of the quasiparticle gap. This reflects the long-range nature of the self-energy, as will be discussed in more detail later. For the BSE calculations, and the nature of the excitons, on the other hand, a finer in-plane mesh is important. The in-plane lattice constant is chosen as $a = 3.32$ Å in the $P\bar{6}m2$ space group, which corresponds to an AA stacking of the trigonal prism unit cell in each layer. The stacking is irrelevant since we focus on the noninteracting monolayer limit. The c lattice constant is varied to study the convergence. The in-plane lattice constant is taken from the Materials Project [32,33] and was optimized in the GGA. The convergence with d, the distance between the layers, is a major object of our study and discussed in Sec. III. For the BSE steps of the QS$G\hat{W}$ calculations in Secs. III A and III B, we use six valence and six conduction bands but we checked that the results differed from those of 10 valence and 10 conduction bands by only 30 meV. Note that there are six Se-p and two occupied W-d states, so this includes more than the relevant atomic orbitals and corresponds to a range of at least 8 eV in the valence and conduction bands, which proves to be sufficient to get the dielectric function and band structure adequate in the range we study. Our calculations do not include electron-phonon band gap zero-point motion renormalizations. These were studied by Mishra *et al.* [34] and were found to be only 30 meV.

III. RESULTS

A. Quasiparticle bands and band gaps

First, we explore the electronic structure at different levels of theory (DFT, QSGW, and QS$G\hat{W}$) for several interlayer distances d. The band gap is found to be direct with the VBM (valence band maximum) and CBM (conduction band minimum) at points K and $-K$. Figure 1 shows the DFT, QSGW, and QS$G\hat{W}$ band structure for $d = 25$ Å specified by blue, red, and green, respectively. The band gap changes from 1.53 eV in LDA to 2.95 eV and 2.71 eV in QSGW and QS$G\hat{W}$, respectively, using the converged $9 \times 9 \times 3$ mesh. In QS$G\hat{W}$, including the electron-hole coupling through the ladder diagrams in the calculation of the polarization propagator P reduces $W = (1 - Pv)^{-1}v$ to $\hat{W}$. Hence, the self-energy $\Sigma = iG\hat{W}$ and the gap are also reduced. We note that $(E_g^{QS G\hat{W}} - E_g^{LDA})/(E_g^{QSGW} - E_g^{LDA}) \simeq 0.83$, which shows that the reduction of the gap is in good agreement with the empirical approach of hybrid QSGW (h-QSGW), which proposes to reduce the QSGW self-energy by a universal factor of ~0.8. This approach was found to lead to good agreement with experimental band gaps for several materials [26,35].

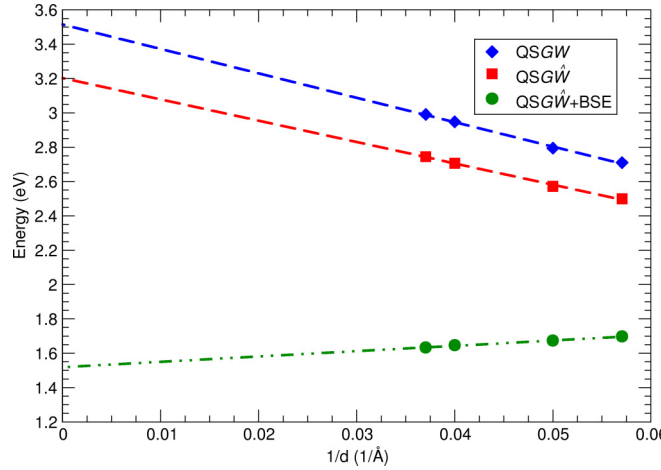

FIG. 2. Band gaps in QSGW, QS$G\hat{W}$ and QS$G\hat{W}$+BSE (optical gap) as a function of the inverse interlayer distance using a $9 \times 9 \times 3$ **k** mesh. Dashed lines show the linear fitting to estimate the band gap at $1/d = 0$.

To attain the strict monolayer limit, we change the interlayer distance from 17.5 Å up to 27 Å and examine the band gaps using different **k**-mesh samplings. Our results show that it is only for the $9 \times 9 \times 3$ and $8 \times 8 \times 3$ **k** mesh that we can see a clear linear trend for the gap as a function of $1/d$. One expects a slow $1/d$ convergence because of the long-range nature of the screened Coulomb interaction [6]. Figure 2 shows the band gaps versus $1/d$ for the $9 \times 9 \times 3$ **k** mesh. We note that although the cell is quite large in the direction perpendicular to the plane, the long-range nature of the self-energy requires us to take more than one **k** point in that direction to achieve convergence. As shown in Fig. 2, QSGW and QS$G\hat{W}$ band gaps converge quite slowly with d, such that in the limit of infinite d, the extrapolated band gaps are around 3.5 and 3.2 eV, respectively, which are about 0.7 eV larger than the corresponding gaps at $d = 17.5$ Å.

We note that the slope of the QS$G\hat{W}$ band gap as a function of $1/d$ is slightly smaller than that of the QSGW. They differ in slope by about 14%. This is a secondary effect. While $\hat{W}$ is decreased with respect to W by increased screening due to electron-hole effects, the rate at which this is changed by inserting larger vacuum regions in between the actual layers, which lowers the effective dielectric constant of the overall system, is not easy to predict. In other words, this would require studying how the electron-hole interactions change as a function of the dimensionality of the system or the reduced

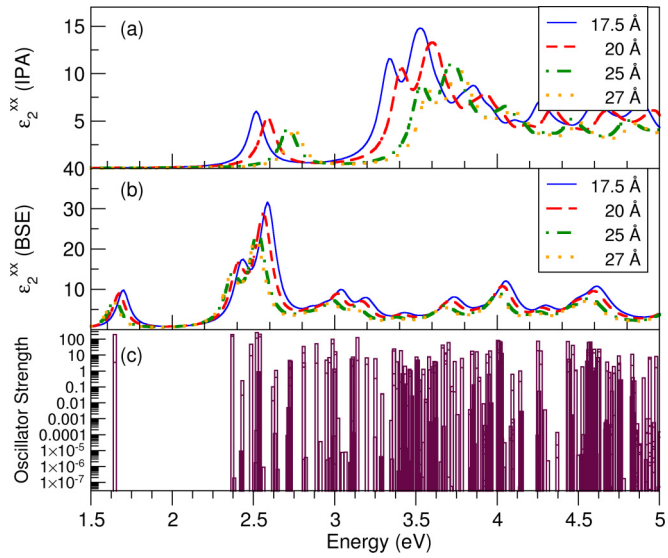

FIG. 3. (a), (b) Imaginary part of the macroscopic dielectric function tensor $\epsilon_2(\omega)$ for x polarization within the IPA and BSE, respectively; shown for four interlayer distances; (c) Oscillator strengths along x associated with the excitonic states from the BSE on a logarithmic scale for interlayer distance 27 Å.

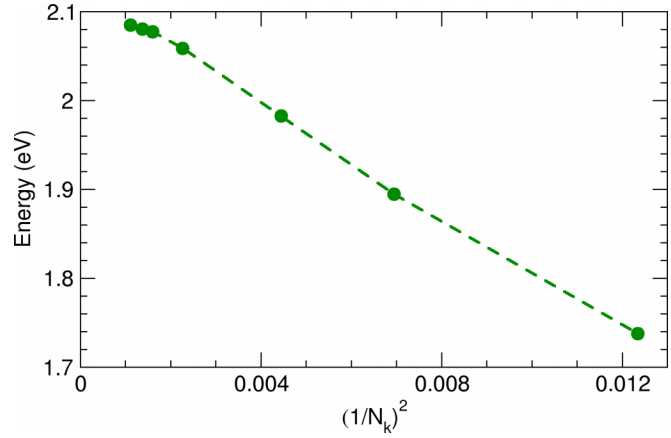

FIG. 4. Energy of the lowest exciton as a function of the inverse of the number of **k** points squared for $d = 20$ Å with $N_v = N_c = 4$.

and distance dependent screening in a 2D system. At this point, we can only point out that there does seem to be a dependence but we cannot yet provide a theoretical insight into its origin.

B. Optical response

In this section, we turn to the optical absorption, which is closely related to the imaginary part of the dielectric function $\varepsilon_2(\omega)$. Figures 3(a) and 3(b) show $\varepsilon_2(\omega)$ for several interlayer distances as calculated in the independent particle approximation (IPA) and in the BSE. The former omits both local field and electron-hole interaction effects and corresponds to vertical transitions between the bands. These calculations have been done using the QS$G\hat{W}$ bands as inputs, and the photon polarization was chosen to be along the x direction. By symmetry, the macroscopic dielectric function is isotropic in the xy plane and we are primarily interested in the in-plane polarization. For the BSE calculations shown in Fig. 3(b), we include six valence and six conduction bands in the two-particle Hamiltonian on a $9 \times 9 \times 3$ **k** mesh. We use the Tamm-Dancoff approximation, which has been shown to be valid in a wide range of materials [36]. The spectrum is broadened by including an imaginary part which linearly increases with energy. Although there is an overall redshift of the spectrum, one can see that the difference between the IPA and BSE does not amount to a simple shift toward lower energies, but instead, BSE significantly modifies the shape of the spectrum. Moreover, in BSE a sharp peak occurs below the quasiparticle gap, which corresponds to the first bright exciton. The position of the various peaks in $\varepsilon_2(\omega)$ does not exhibit significant variation with respect to the interlayer distance. In particular, unlike the QSGW gaps which change strongly with the size of the vacuum region, the position of the first peak or the optical gap stays practically constant for this **k** mesh. This indicates an increasing binding energy with the size of the vacuum region, as expected, given the long-range nature and decreasing screening of the screened Coulomb interaction W as the interlayer distance increases. This is shown also in Fig. 2, which shows that the optical gap is nearly constant as a function of interlayer distance within the range of distances shown. In fact, it appears to slightly decrease with layer distance, but this variation is within the error bar of the calculations. Furthermore, as we discuss in the next section, the exciton peak is sensitive to the **k**-mesh sampling. In the results shown in Fig. 2, the mesh is kept fixed at the same mesh as used in the QS$G\hat{W}$ band calculation, and provides only a lower limit of the optical or exciton gap.

Figure 3(c) shows the oscillator strengths for all eigenvalues of the two-particle Hamiltonian on a log-scale at $d = 27$ Å. Only the levels with highest oscillator strength in (c) show up as peaks in (b). The oscillator strengths here are not normalized and thus only the relative intensity between different levels has physical meaning.

C. Convergence of exciton gap

To converge the energy of the first exciton peak, it is necessary to use a finer **k** mesh, since it is localized in **k** space. On the other hand, as we will show in Sec. III E, for the lowest excitons, we can restrict the active space of bands to fewer valence and conduction bands included in the BSE. Figure 4 shows the exciton gap as a function of $1/N_k^2$, where N_k is the total number of **k** points in the 2D mesh. The interlayer distance is $d = 20$ Å, which is close to the converged monolayer limit. In fact, as mentioned earlier, from Fig. 2 the BSE-calculated lowest exciton peak does not vary significantly with d. Here we use $N_v = N_c = 4$, where N_v and N_c specify the numbers of valence and conduction bands used in BSE, respectively. For the direction normal to the plane, three **k** points are used. The optical gap for the isolated monolayer limit and for $N_k \to \infty$ is thus found to be ∼2.1 eV, whereas the quasiparticle gap in that limit is

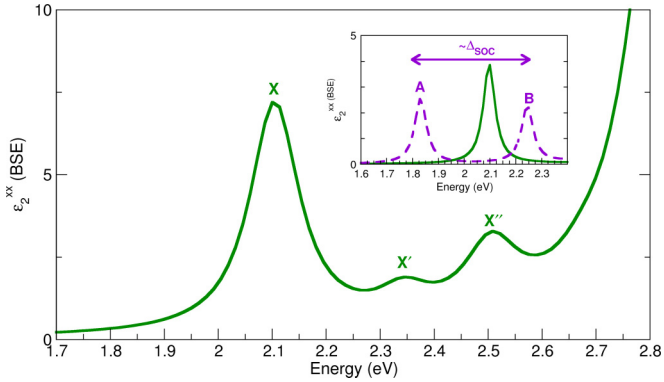

FIG. 5. Imaginary part of the macroscopic dielectric function tensor $\epsilon_2(\omega)$ for x polarization within the BSE using one valence and one conduction band on a $30 \times 30 \times 3$ **k** mesh. Label X shows the ground state exciton without SOC, known as $1s$. X′ shows the second bright exciton, known as $2s$. A third prominent peak also appears, which is labeled as X″. The inset shows the splitting of the X exciton due to SOC into two excitons commonly known as excitons A and B. The spectrum is shifted so that the energy of the first peak coincides with the converged value of 2.1 eV.

found to be 3.2 eV, implying an exciton binding energy of 1.1 eV.

D. Discussion of the exciton spectrum in relation to prior theory work and experiment

Figure 5 shows $\varepsilon_2(\omega)$ in the BSE as in Fig. 3(b), for $d = 25$ Å, but with a finer **k** mesh of $30 \times 30 \times 3$ with $N_v = N_c = 1$. This finer mesh provides us with a better picture of the profile of the spectrum below and just above the quasiparticle gap. We can readily notice that compared to Fig. 3(b), more weight is shifted to the first peak, making it the strongest optical excitation.

Table I shows some of the experimental and theoretical results for the energy of the A (first bright) exciton, its binding energy and the energy splitting between A and the A′(second bright) exciton. To compare our results here with experiments and other theory works in the literature, it is important to include SOC effects. The QUESTAAL QSGW and BSE codes do not yet allow us to fully include the spinorial nature of the wave functions in the Green's functions. However, we can include the spin-conserving L_zS_z part of the SOC in the GW parts, and add the remaining SOC terms perturbatively in the subsequent band calculations. Doing so, we obtain the splitting of the QSGW bands which can then also be used in the BSE optical calculation. This gives the results shown in the inset of Fig. 5, and is compared to the calculation without SOC for the first peak. We can also include SOC perturbatively in our QS$G\hat{W}$ calculations. In other words, we add the SOC Hamiltonian to the QS$G\hat{W}$ Hamiltonian matrix in the LMTO basis set and rediagonalize it. Adding SOC splits the lowest exciton peak into the A and B excitons, which results from the SOC splitting of the highest valence and lowest conduction bands at and around the K point [37]. Our results show that at the K point, the valence band splitting is about 445 meV, with the VBM-B going 225 meV down and the VBM-A 219 meV up in energy. However, the CBM, which has a much smaller splitting, also shifts down for both spin directions by about

TABLE I. A exciton energy, A exciton binding energy and A-A′ energy splitting of monolayer WSe_2 as reported in several experimental and theoretical studies (PL: photoluminescence, EELS: electron energy loss spectroscopy)

	Method	Optical gap (eV)/E_b (meV)	A-A′ splitting (meV)
hBN/ML-WSe_2/hBN [41]	Magneto-PL	1.727/170	131
hBN/ML-WSe_2/hBN [42]	Magneto-PL	1.712/172	131
ML-WSe_2/Si/SiO_2 [43]	Linear absorption and two-photon PL	1.65/370	160
hBN/ML-WSe_2/hBN [44]	Magnetoabsorption	1.723/161	130
hBN/ML-WSe_2/hBN [45]	Gate-dependent reflection and PL	~1.72/-	120
hBN/ML-WSe_2/hBN [46]	Magneto-photocurrent	1.725/168.6	128.6
hBN/ML-WSe_2/hBN [47]	EELS	1.697/-	-
ML-WSe_2/Si/SiO_2 [48]	PL and reflectance	1.744/-	-
ML-WSe_2/PC [49]	Absorption	~1.66/710	200
ML-WSe_2 [8]	Momentum-resolved EELS	1.69/650	-
ML-WSe_2/Si/SiO_2 [50]	1- and 2-photon PL excitation	$1.75/600 \pm 200$	150
ML-WSe_2/SiO_2 [51]	Reflectance	1.67/-	-
hBN/ML-WSe_2/hBN [52]	PL	~1.75/-	-
ML-WSe_2/hBN/n-doped Si [53]	Photoemission	$1.73/390 \pm 150$	-
hBN/ML-WSe_2/hBN [54]	Magnetoabsorption	1.722/-	-
ML-WSe_2 [39]	GW-BSE	1.52/900	-
ML-WSe_2 [38]	GW-BSE	~2.1/596	-
ML-WSe_2 [38]	GW-BSE-Pert. SOC	~1.8/533	140
ML-WSe_2 [38]	GW-BSE-SOC	~1.7/550	140
ML-WSe_2 [55]	LDA+GdW[1]+BSE+SOC	1.76/-	-
ML-WSe_2 [39]	G_0W_0+BSE+SOC	1.52	
ML-WSe_2 [50]	GW_0+BSE	~2	
ML-WSe_2 [57]	GW+BSE	1.78/620	-

[a]Explained in Ref. [56].

0.035 eV. Including these *a posteriori* SOC effects, the A exciton in our results is placed at ∼1.8 eV, which is in excellent agreement with results from Ref. [38]. These authors include SOC fully as well as perturbatively and it is with the latter that we have the best agreement. Numerous experimental results also place the A exciton at about 1.7–1.8 eV, whereas some older theoretical calculations [39] find it near 1.5 eV. In Fig. 5, we label our exciton peaks as X, X′, and X″ to indicate that they do not include SOC. Each would split into an A and B peak when SOC is added.

Our calculated binding energy of ∼1 eV is slightly higher than previously reported values. Ramasubramaniam [39] obtains a gap of 2.42 eV at K, but his calculation includes SOC. If we compare with the average of the SOC-split states, his quasiparticle gap would be 2.67 eV but this is at an interlayer separation $d = 15$ Å. Furthermore, this author obtained a lower indirect K-Λ gap from the valence band at K to a secondary valley in the conduction band along the Γ-K axis, Λ. In Fig. 2, the smallest distance we consider is 17.5 Å and it already gives a slightly higher gap. Our extrapolated quasiparticle gap for infinite distance is significantly higher. Ramasubramaniam's lowest exciton peak occurs at 1.52 eV for the A exciton and 2.00 eV for the B exciton, showing that this splitting simply corresponds to the corresponding valence band SOC splitting at K. His exciton binding energy is thus reported as 0.9 eV using a **k** mesh of $6 \times 6 \times 1$. We can see that our exciton binding energy is only slightly higher than his, while our optical gap and quasiparticle gap are both significantly higher but in better agreement with [38] and experiment.

Most of the experimental results in Table I refer to WSe_2 layers encapsulated or influenced by a substrate. Only the q-EELs results of Hong *et al.* [8] correspond to freestanding monolayers. The main point is that the exciton gap itself is largely independent of the substrate or encapsulation, but the quasiparticle gap and hence the exciton binding energy is not. The exciton binding energy in Ref. [8] is estimated by comparing the optical exciton gap with a GW_0 calculated quasiparticle gap and thus the discrepancy between their 650 meV and our larger exciton binding energy stems from the different extrapolated quasiparticle gap, which is larger in our calculation.

Moreover, Fig. 5 shows that between the lowest exciton and the quasiparticle gap, other peaks occur. By examining the oscillator strengths, we see that there are also several dark excitons in this region as shown in Fig. 3(c). We identify the next bright exciton which is slightly lower in intensity but clearly visible in $\varepsilon_2(\omega)$ in Fig. 5 as the X′ exciton, which, in the literature, is usually associated with either a $2s$ or $2p$ type exciton using the hydrogenic Rydberg series nomenclature. Whether $2s$ or $2p$ are showing up in experiment depends on the experimental probe used: two-photon absorption reveals the $2p$ excitons, while linear absorption or luminescence reveals the 2s excitons. This arises from the different matrix elements and symmetry selection rules. We should note that this classification does not imply a strict hydrogenic Rydberg series, because the system is 2D rather than 3D and the screened Coulomb potential does not behave simply as $1/\varepsilon r$ since the screening in 2D is strongly distance dependent [40]. Furthermore, a $2p$ type exciton having an envelope function which has nodes would be dark in the $\varepsilon_2(\omega)$ spectrum but accessible in two-photon absorption experiments. Adding SOC will split this peak into the two A′ and B′ peaks. Following our previous discussion of including SOC effects, We expect the splitting between A and A′ to stay almost the same as X and X′, since we associate them to s-like states. We call the next peak X″, which is close to X′ in energy but relatively higher in intensity. We also caution that the details of the exciton spectrum shown in Fig. 5, such as peak splittings and positions depend strongly on the convergence with **k** points. However, qualitatively, Fig. 5 is in good agreement with the results of Ref. [38] without SOC and shows the same relative intensities for X, X′, and X″. In particular, our X-X′ splitting is about 255 meV which is very close to the reported value of 215 meV by [38] for a $39 \times 39 \times 1$ **k**-mesh sampling. This value is higher than the values in Table I, which the authors contribute to the substrate effects used in experiments. These authors also report a value of 140 meV using a coarser **k** mesh, which is closer to experimental results.

We conclude that both convergence as a function of **k** mesh and vacuum thickness plays an important role. This was also concluded by Qiu *et al.* [11] in the case of MoS_2. These authors in fact dealt with the monolayer separation by using a truncated Coulomb potential and used an even finer **k** mesh. Their use of a truncated Coulomb interaction allows for an easier convergence to isolated monolayers and they compare the screening dielectric constant with the strict 2D Keldysh limit [1].

E. Exciton wave function analysis

1. Overview

To better understand the nature of excitons, we can analyze the **k**-space and real-space distribution of the first few excitons. First, we calculate $A_\lambda^{v,c}(\mathbf{k}) = \langle v, c, \mathbf{k}|\Psi_\lambda^{Ex}\rangle$ for a particular band pair $\{v, c\}$ along several high-symmetry paths in the BZ where λ denotes the excitonic eigenstate. Here we focus on the first few excitons by separately considering the ranges of energies which include only $\lambda = 1, 2$ (degenerate-bright), $\lambda = 3$ (dark), $\lambda = 4$ (dark), $\lambda = 5, 6$ (degenerate-semi-bright), $\lambda = 7, 8$ (degenerate-semi-bright) and $\lambda = 21, 22$ (degenerate-bright). We should note that bright excitons $\lambda = 1, 2$, $\lambda = 5, 6$ and $\lambda = 7, 8$ correspond to X, X′, and X″ peaks in Fig. 5, respectively.

In this section, we use $N_v = 1$, $N_c = 1$, which allows us to use a finer **k** mesh. This will be justified in Sec. III E 2; however, we have explicitly checked that $N_v = 1, N_c = 1$ give essentially the same results for the exciton region below the quasiparticle gap as $N_v = 4, N_c = 4$ for the smaller **k** meshes used. For studying the overall $\varepsilon_2(\omega)$ up to higher energies in the continuum, it is important to include more bands but this limits the number of **k** points we can afford. When focusing on the excitons, the opposite is true and the important convergence parameter is the number of **k** points.

Figure 6 in Sec. III E 2 shows the band weights of various excitons. For each λ, we show the weight $W_\lambda^c(\mathbf{k}) = \sum_v |A_\lambda^{vc}(\mathbf{k})|^2$ at each **k** by the size of the colored circle on the conduction band c and likewise we use $W_\lambda^v = \sum_c |A_\lambda^{vc}(\mathbf{k})|^2$ for the weight on the valence band. The colors only distinguish between different bands and have no physical meaning.

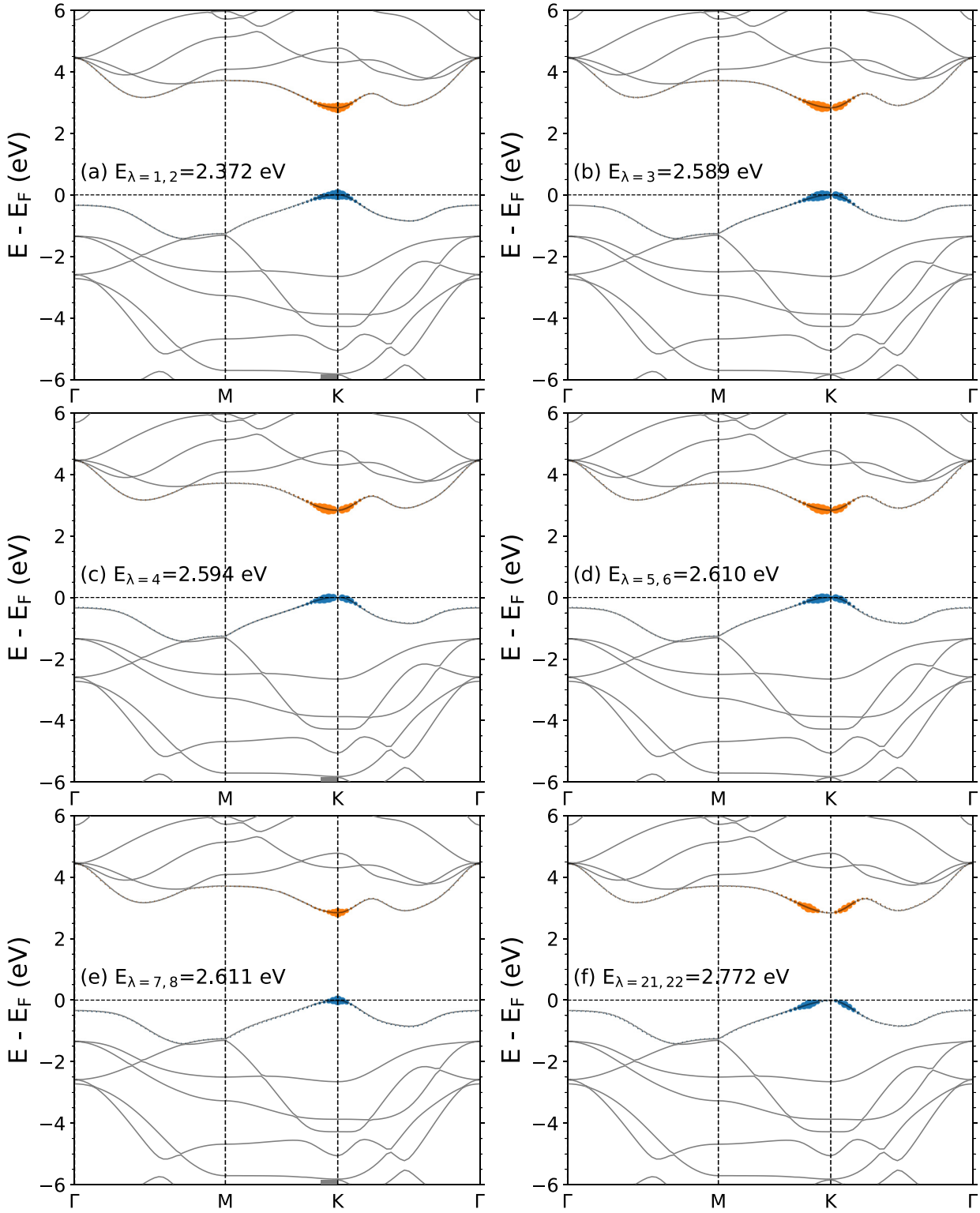

FIG. 6. Weights of the exciton wave function along high-symmetry paths, contributed by different bands (a)–(f) for six excitonic eigenvalues. The size of the colored circles indicates the exciton weight as explained in the text. The colors have no meaning and only serve to distinguish different bands.

Next, in Sec. III E 3, we investigate $A_\lambda^{v,c}(\mathbf{k})$ for a particular exciton and band pair as a function $\mathbf{k}$ on a mesh of $\mathbf{k}$ points. These exciton expansion coefficients $A_\lambda^{v,c}(\mathbf{k})$, in fact, are the Fourier transforms of slowly varying envelope functions within the Wannier-Mott $\mathbf{k}\cdot\mathbf{p}$ theory of excitons [11]. This slowly varying envelope function would be a hydrogenic function in the case of a 3D isotropic system, and the full real-space exciton wave function is found from this envelope function modulated by the product of the Bloch functions at the valence and conduction bands at the $\mathbf{k}$ point where the

exciton is centered. Here, they are 2D analogs and somewhat distorted by the anisotropies. In 2D, the angular behavior of the envelope function is described by the 2D Laplacian equation, which has solutions of the form $\cos m\phi$ and $\sin m\phi$ with $m = 0,\ 1,\ 2,\ \ldots$, and are referred to as $s,\ p,\ d,\ \ldots$ in analogy with the 3D case. The general solution $e^{im(\phi-\phi_0)}$ contains an arbitrary phase, resulting from the overall arbitrary phase of the eigenstates of the two-particle Hamiltonian diagonalization, but this only affects the orientation of these exciton wave functions in **k** space. This 2D behavior is valid as long as the slowly varying potential for which the slowly varying envelope function is a solution of the effective Schrödinger equation, is indeed axially symmetric. This is true for the **k** points close to point K in the region contributing to the exciton. Beyond a certain distance in **k** space, one might expect a trigonal warping. The real-space excitons at short distance thus will not show a circular but rather hexagonal shape. Conversely, the less strongly bound excited excitons are more spread in real space and hence more localized in **k** space, in the region where circular symmetry is valid. The main advantage of this analysis is that it shows us the sign changes of the envelope function as a function of the angle and hence the angular patterns, which can explain why certain excitons are dark.

Finally, we will examine the excitons fully in real space in Sec. III E 4. In that case, we look at $|\Psi(\mathbf{r}_h, \mathbf{r}_e)|^2$, where we can either fix the hole at $\mathbf{r}_h$ or the electron at $\mathbf{r}_e$, and then plot the probability distribution of the other particle. Since the valence and conduction bands, from which the excitons are derived, are all mainly W-d like, either choice is equally good and we choose to fix the hole. This distribution will show both the large scale envelope function behavior and the local atomic orbital character.

Before we present our exciton analysis results, let us mention that our discussion of bright and dark excitons here is limited to the singlet excitons. Excitons can also be dark due to the spin structure as was discussed for WSe_2 and MoS_2 by Deilman *et al.* [55]. The darkness of excitons considered here is rather related to the excited nature of the excitons in the Rydberg series, and their slowly varying envelope function in a Wannier-Mott exciton model.

We also note that all bright excitons are doubly degenerate and all dark excitons are singly degenerate. The double degeneracy of the first bright exciton results from the equal contributions at K and $-K$. These are related by time reversal symmetry and hence, there is a Kramers degeneracy. Their double degeneracy can also be understood from the symmetry analysis of Song *et al.* [58]. In fact, the exciton is expected to be localized near the W atom since the top valence and bottom conduction bands are both dominated by W orbitals. The excitons can thus be classified according to the symmetry of the W site which is the full symmetry D_{3h} of the crystal. Because we focus on excitons with polarization in the plane, this immediately tells us that all bright excitons will be doubly degenerate and correspond to the E' representation. Dark excitons which are symmetric with respect to the horizontal mirror plane (as we find to be the case for all the ones we examined) must thus correspond to the A_1' or A_2' irreducible representations which are both non-degenerate. The distinction between the two is whether they are even or odd with respect to the vertical mirror planes and or twofold rotations in the plane.

2. Band weights

Figure 6 shows the band weights for various excitons. We can clearly see that almost all the contribution comes from the pair of the highest valence and lowest conduction bands focused on or around point K in the Brillouin zone and decaying as we move away from K in an anisotropic way. For example, the conduction band has a larger mass along the KM than the $K\Gamma$ direction and the exciton spreads out further along the KM direction. We can explain this in terms of the Wannier-Mott hydrogenic model of the exciton. First, indeed, the localization in **k** space implies a large spread in real space consistent with the Wannier-Mott type exciton. Second, within this model the effective Bohr radius of the exciton is inversely proportional to the band effective mass and hence gives a smaller Bohr radius in real space for the MK direction which corresponds to a larger spread in **k** space. Figures 6(b) and 6(c) demonstrate the weights for the second and third excitons in energy, which are $|A^{vc\mathbf{k}}_{\lambda=3}|$ and $|A^{vc\mathbf{k}}_{\lambda=4}|$, respectively. For these two dark and nondegenerate excitons, we can clearly see that almost all the contribution still comes from only the pair of the highest valence and lowest conduction bands focused around point K in the Brillouin zone but now with a zero value at point K itself, in clear contrast to the first bright exciton where the contribution at point K is the largest, as shown in Fig. 6(a). Figure 6(d), shows the weight $|A^{vc\mathbf{k}}_{\lambda=5}|$, $|A^{vc\mathbf{k}}_{\lambda=6}|$, which corresponds to fourth exciton in energy, doubly degenerate and semibright, *i.e.,* less bright than the first bright exciton. This exciton has characteristics in between those of the previous bright and dark excitons, with an overall distribution like the dark excitons but nonzero contribution at point K. Figure 6(e) corresponds to fifth exciton in energy which resembles the first bright exciton in oscillator strength but less extended around K. Figure 6(f) shows the excitonic weights for an exciton with relatively higher energy, which in its **k**-space distribution, resembles the dark excitons, even though it has a strong oscillator strength. In **k** space, we also see it has larger dip at and around point K.

3. k-space analysis

To explain the behaviors noted in Sec. III E 2, we need to fully examine the **k**-space relations of $A^{vc}_{\lambda}(\mathbf{k})$ instead of only looking at their absolute values along high-symmetry lines. Because the bright excitons are doubly degenerate, any linear combination of the two eigenstates is also an eigenstate and this makes it difficult to visualize them. Thus, in this section we focus on the dark excitons.

In Fig. 7 we show the real, imaginary, and absolute values of the envelope function $A^{vc}_{\lambda}(\mathbf{k})$ for the first two dark excitons over the 2D **k** space in one unit cell as a color plot. Top and bottom rows correspond to $\lambda = 3$ and $\lambda = 4$, respectively. This requires an even finer **k** mesh but we can now restrict the v and c to just the valence and conduction band edges and thus afford to have a 30×30 mesh in the plane. In spite of the rather coarse pixelation, we can see that around both points K and $K' = -K$, there is a threefold symmetry with alternating positive and negative signs as we go around the

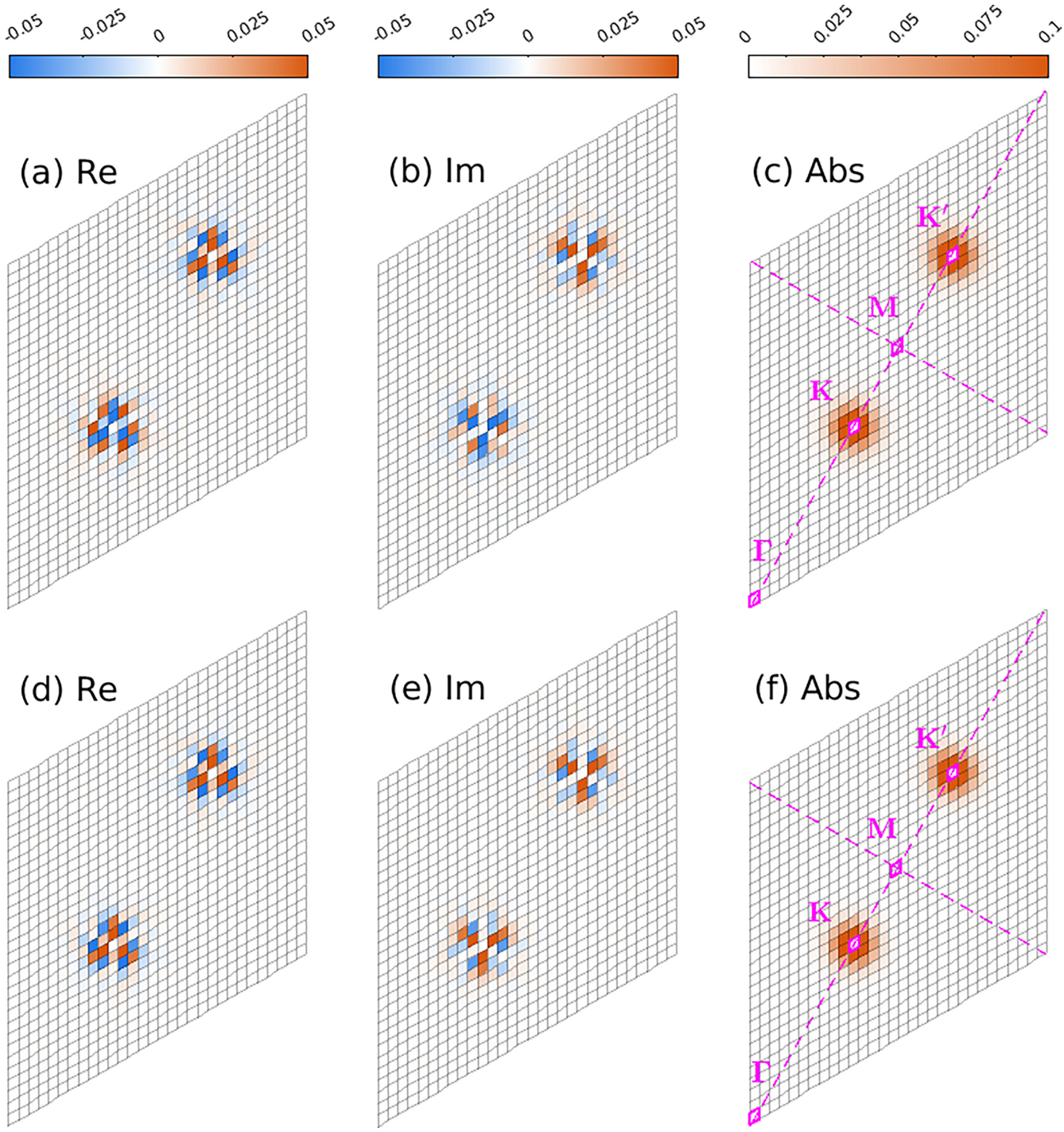

FIG. 7. Real, imaginary and absolute values of the envelope function $A^{\lambda}_{vc\mathbf{k}}$ for the first two dark excitons over the **k** space. First and second rows belong to $\lambda = 3$ and $\lambda = 4$, respectively. High symmetry points are labeled as magenta in the absolute value panel, as reference.

central point K or K'. In between we may see a white line of pixels indicating a node. This indicates a $\cos(3\phi)$ type of behavior for the envelope function. There appears to be a slight offset of the nodal lines from the symmetry directions but this arises from an arbitrary overall phase of the two particle eigenstates. Considering that the matrix elements of the velocity operator in the plane are fully symmetric around K, these sign changes indicate that the exciton will be dark by the modulation of the threefold symmetry envelope function. Furthermore, we can see that for the $\lambda = 3$ exciton the signs of the **k**-space envelope function are opposite near K and K' or more precisely the function is odd with respect to a vertical mirror plane going through the $\Gamma - M$ line while for $\lambda = 4$ the signs are the same. So, as mentioned before, we conclude that exciton $\lambda = 3$ can be described as an A'_2 exciton while $\lambda = 4$ is an A'_1 exciton. However, both become dark by the threefold symmetry of the envelope function around K and K'.

As already discussed in Sec. III E 1, a $\cos(m\phi)$ behavior is expected but the question arises why we only see a $m = 3$ or f-like envelope function for these lowest energy

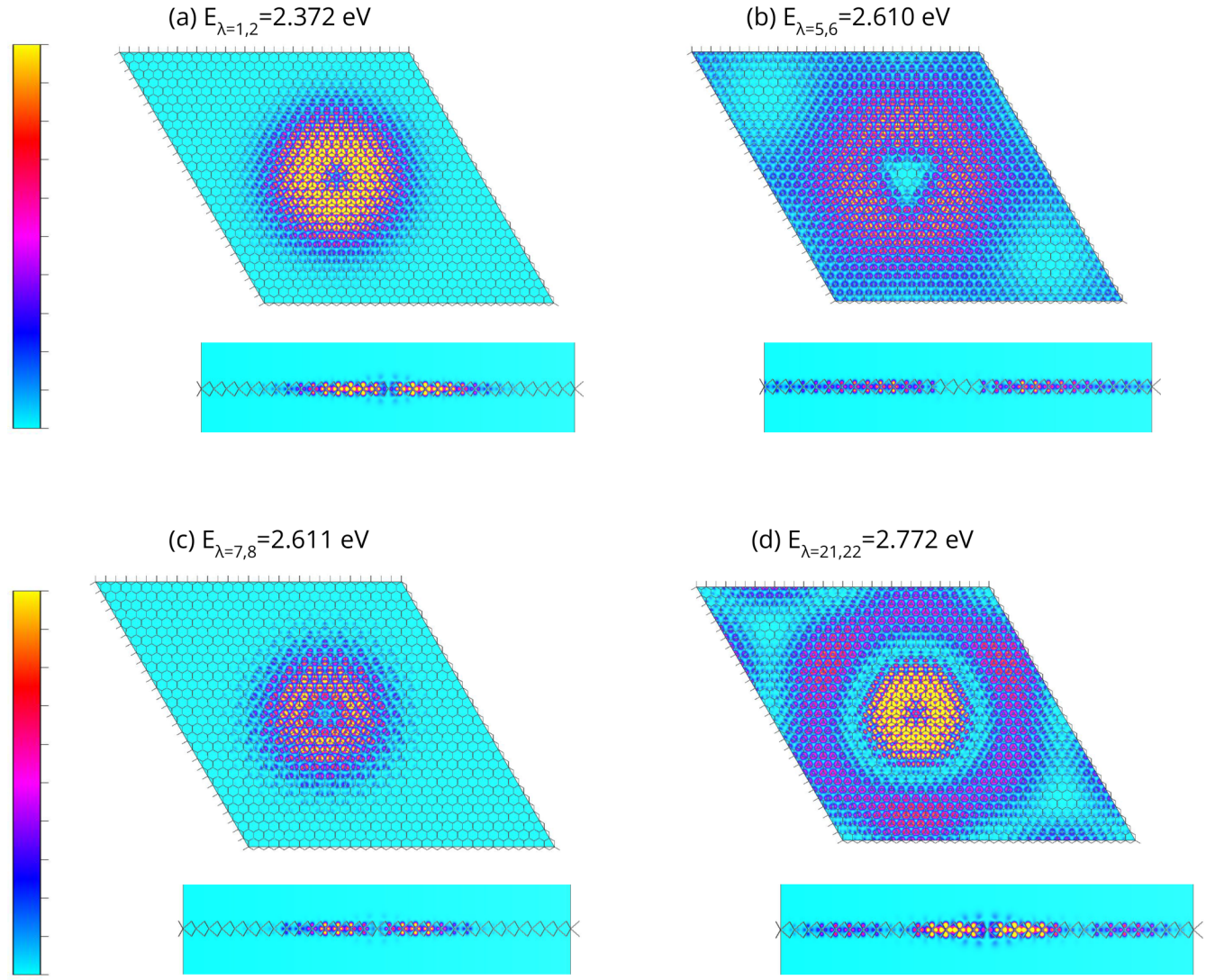

FIG. 8. Real-space probability density of the first three bright excitons along with one higher energy bright exciton, shown for a section that goes through the tungsten atoms in the middle, perpendicular (top), and parallel (bottom) to the out-of-plane axis, respectively. For the color bar limits, the same minimum (cyan) and maximum (yellow) values are used in all maps. Values smaller (larger) than this range are shown by the saturation colors cyan (yellow).

dark excitons. States with lower m are indeed expected but would be more spread out in real space (the higher the angular momentum, the more localized by the centrifugal term (of the form m^2/r^2) and hence more localized in momentum space; therefore, in order to access p-like or d-like states originating from and around point K, as reported in Ref. [11] for MoS_2, we would need a much finer **k** mesh to capture the fine structure around this point. With the **k** mesh used in this study, we only access points in momentum space which are not close "enough" to K responsible for p- or d-like states.

Our analysis in terms of the envelope function resembles the approach used by Qiu *et al.* [11] for MoS_2. However, they used a special dual mesh approach, which allowed them to use **k** meshes as large as 300×300. With our 10 time smaller divisions we still obtain a rather pixelated view of the **k** space behavior. Therefore we can unfortunately not obtain the nodal structure near each point K as accurate. The effective k spacing $(2\pi/a)/30$ is about 0.06 Å^{-1} but the size of the exciton spread itself is of order 1 Å^{-1} and thus we do not have sufficient resolution to fully see the fine structure which would reveal the Rydberg like excited states of the exciton. The number of excitons we can resolve also depends strongly on the fineness of the **k** mesh and as mentioned before does not allow us to capture the p or d-like excitons.

4. Real-space analysis

Next, we turn our attention to the real-space spread of the exciton wave functions. In Figs. 8 and 9, we visualize the exciton wave functions in real space as a colormap. The interlayer distance of 25 Å is used for the calculations of this section.

Each panel shows the spatial distribution of one exciton, on a section going through the W atoms in the middle of the supercell, perpendicular to the out-of-plane axis (top) and perpendicular to the in-plane axis (bottom). Figure 8(a) corresponds to the lowest energy exciton. As we can see,

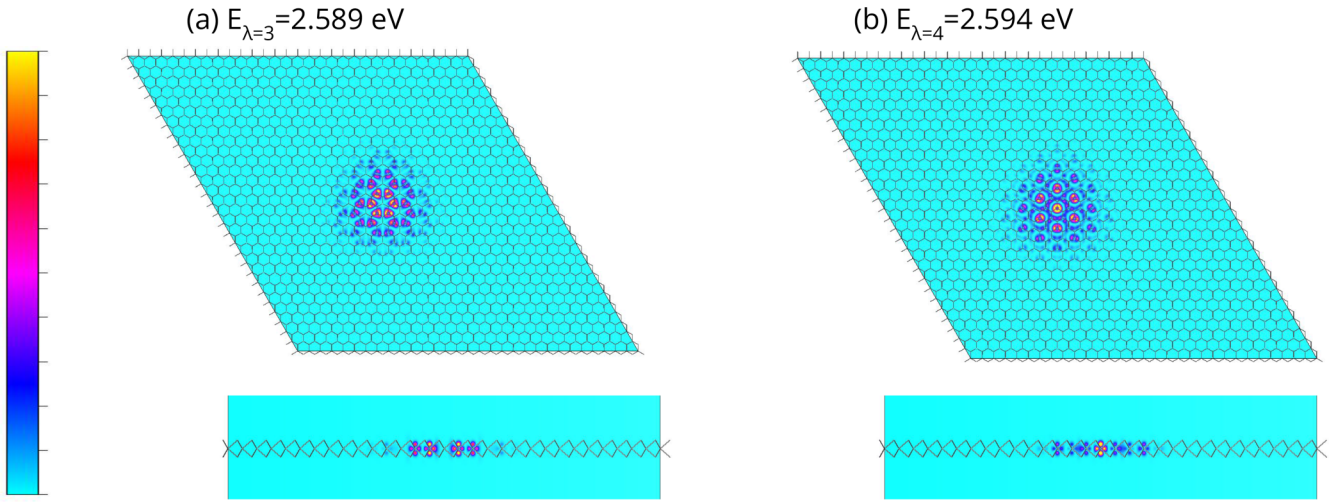

FIG. 9. Real-space probability density of the first two dark excitons in energy, shown for a section that goes through the tungsten atoms in the middle, perpendicular (top) and parallel (bottom) to the out-of-plane axis, respectively. For the color bar limits, the same minimum (cyan) and maximum (yellow) values are used in all maps. Values smaller (larger) than this range are shown by the saturation colors cyan (yellow).

the overall shape resembles the hexagonal symmetry of the structure rotated by 60°, such that the highest weight (yellow) lies on a hexagonal region extending from two to four unit cells away from the hole. Looking closer, we can see that the symmetry is actually 3-fold consistent with the three-fold symmetry of the W site. Also, around each W atom, a dumbbell-like distribution of the electron density can be seen, which originates from the d orbitals of the individual W atoms. This can be best seen in the edge-on projection, which clearly shows d-orbital shapes. The orientation of this dumbbell-like distribution changes locally going from one edge of the hexagon to the other.

For the two dark excitons, we see a different character shown in Fig. 9. In Fig. 9(b), the distribution intensity is the highest around the W atom in the center, while in Fig. 9(a), it is almost zero around W in the center. Furthermore, in Fig. 9(a), we see clear nodal lines at 120° from each other, reminiscent of the $\cos(3\phi)$ pattern in the **k**-space figure. In Fig. 9(b), we still see regions of low values in rings around each atom but still showing some threefold symmetry. However, their overall sizes in the real space are pretty close to each other and somewhat smaller than the previous bright exciton. On the other hand, for the next bright exciton shown in Fig. 8(b), the spread out is substantially farther. As mentioned before, as the exciton energy approaches the gap and the exciton binding energy is reduced, the exciton spreads further in real space.

Interestingly, even for the lowest energy bright exciton, the envelope function is not at its maximum in the center but is rather ring shaped with a dip in the very center. In the second bright exciton, shown in Fig. 8(b), the central region is distinctly triangular shaped and corresponds to a larger central region with very low value. The spatial extent of this exciton is significantly larger than the first bright exciton, consistent with the 2s character. These features can be explained in terms of the 2D envelope functions which correspond to the electron-hole attraction potential. Because of the 2D screening being very distant-dependent, it behaves like a weak logarithmic potential $\ln(r)$ near the origin and as an unscreened $1/r$ potential far away [2]. The solutions for the 2D Schrödinger equation with a logarithmic potential were studied by Atabek, Deutsch, and Lavaud [59]. Because of the weak logarithmic potential, the $m = 0$ (or s-like states) do not start as r^0 or a constant but more like r as can be seen in Fig. 4 of [59]. They go through a single maximum at finite r consistent with the ring shaped envelope we see. For the 2s state, there is a node but the onset starts not at $r = 0$ but at finite r. The stronger unscreened Coulomb interaction at large distance means that excited states like 2s states are pushed out to larger r. This is consistent with the large triangular hole in this exciton wave function in Fig. 8(b). The triangular shape at close distance in real space results from the triangular warping of the bands involved in **k** space at large **k**. Even for the lowest exciton, the center region is triangular rather than circular.

The next bright exciton, shown in Fig. 8(c) shows very similar behavior as the first bright exciton. We recall that the doubly degenerate exciton labeled $\lambda = 5, 6$ is the X′ exciton while $\lambda = 7, 8$ corresponds to the X″ exciton. It is somewhat surprising that X″ and X are so similar in spatial extent. However, we can see from Figs. 8(a) and 8(c) that they have different probability densities. We picked the same minimum and maximum values mapped to the color scale for both to facilitate an absolute comparison. They also have somewhat different **k**-space localization: X″ falls off faster with k away from the band edge K than X does, as shown in Fig. 6. Finally, Fig. 8(d) shows the bright exciton with the largest exciton energy discussed in this paper, which has a wider spread and a clear radial node structure.

Overall, the real-space and reciprocal-space exciton wave functions show an interesting variety of behaviors which can largely be understood in terms of the 2D problem with a Keldysh-type distant-dependent screened Coulomb potential.

IV. CONCLUSIONS

In this paper, we presented a study of the band structure and excitons in monolayer WSe_2 using an all-electron muffin-tin-orbital implementation of the QSGW and BSE approaches. The calculations went beyond the usual IPA and RPA based GW by including the electron-hole interaction effects in the screening of W, which is then called $\hat{W}$. As is already well known, the quasiparticle gaps were found to converge slowly as a function of the interlayer distance, as $1/d$ and the replacement of W by $\hat{W}$ essentially provides a downward shift of the gap, which however is not entirely constant but with a smaller slope as a function of $1/d$ for the QS$G\hat{W}$. The exciton spectrum was found to be in excellent agreement with prior theory work [38] and various experiments when SOC corrections of the bands are added. As expected, the excitons show a smaller variation as a function of interlayer distance, as a result of the compensation of the exciton binding energy and quasiparticle gap self-energy shift, which are both proportional to $\hat{W}$. Converged exciton eigenvalues were shown to require a very fine in-plane $\mathbf{k}$ mesh in order to obtain agreement with experimental exciton gaps. The nature of dark and bright excitons was analyzed in terms of their reciprocal space and real space envelope functions and showed distinct behaviors. First, all the excitons examined were derived almost exclusively from the top valence and lowest conduction bands near K. But the dark ones had zero value at K itself. The darkness of two of the excitons was found to result from the threefold symmetry nodal pattern of the envelope function but these two dark excitons still show distinct behavior in real space. The exciton symmetries were analyzed in the context of the Wannier-Mott theory adjusted for 2D. The threefold symmetry of the first dark excitons found here indicates f-like excitons. We expect that there are also p- and d-like envelope functions in a Rydberg-like series, but the reason why the lower angular momenta p- or d-like excitons could not be revealed is related to the limitations in the number of $\mathbf{k}$ points we could include in the BSE. A finer mesh near the band extrema at K and $-K$ is required to capture these excitons which are expected to be more localized in $\mathbf{k}$ space. Among the bright excitons, we were able to identify the A′ exciton and identify it with a $2s$ like exciton state. Our present study provides a detailed look at how the Mott-Wannier model and qualitatively explains the exciton series. However, it shows that the strongly distance-dependent screening of the Coulomb interaction between electron and hole modifies the spatial extent and shape of the exciton envelope functions. These features emerge naturally from the first-principles BSE approach even though we do not explicitly solve for a Wannier-Mott slowly varying envelope function.

Some data related to this work are available [60].

ACKNOWLEDGMENTS

This work was supported by the U.S. Department of Energy Basic Energy Sciences (DOE-BES) under Grant No. DE-SC0008933. Calculations made use of the High Performance Computing Resource in the Core Facility for Advanced Research Computing at Case Western Reserve University.

[1] L. V. Keldysh, Coulomb interaction in thin semiconductor and semimetal films, Pis'ma Zh. Eksp. Teor. Fiz. **29**, 716 (1979) [JETP Lett. **29**, 658 (1979)].

[2] P. Cudazzo, I. V. Tokatly, and A. Rubio, Dielectric screening in two-dimensional insulators: Implications for excitonic and impurity states in graphane, Phys. Rev. B **84**, 085406 (2011).

[3] M. Shinada and S. Sugano, Interband optical transitions in extremely anisotropic semiconductors. I. Bound and unbound exciton absorption, J. Phys. Soc. Jpn. **21**, 1936 (1966).

[4] C. Delerue, M. Lannoo, and G. Allan, Excitonic and quasiparticle gaps in Si nanocrystals, Phys. Rev. Lett. **84**, 2457 (2000).

[5] C. Delerue, G. Allan, and M. Lannoo, Dimensionality-dependent self-energy corrections and exchange-correlation potential in semiconductor nanostructures, Phys. Rev. Lett. **90**, 076803 (2003).

[6] H.-P. Komsa and A. V. Krasheninnikov, Effects of confinement and environment on the electronic structure and exciton binding energy of MoS_2 from first principles, Phys. Rev. B **86**, 241201(R) (2012).

[7] L. Wirtz, A. Marini, and A. Rubio, Excitons in boron nitride nanotubes: Dimensionality effects, Phys. Rev. Lett. **96**, 126104 (2006).

[8] J. Hong, R. Senga, T. Pichler, and K. Suenaga, Probing exciton dispersions of freestanding monolayer WSe_2 by momentum-resolved electron energy-loss spectroscopy, Phys. Rev. Lett. **124**, 087401 (2020).

[9] C. A. Rozzi, D. Varsano, A. Marini, E. K. U. Gross, and A. Rubio, Exact Coulomb cutoff technique for supercell calculations, Phys. Rev. B **73**, 205119 (2006).

[10] F. Hüser, T. Olsen, and K. S. Thygesen, Quasiparticle GW calculations for solids, molecules, and two-dimensional materials, Phys. Rev. B **87**, 235132 (2013).

[11] D. Y. Qiu, F. H. da Jornada, and S. G. Louie, Screening and many-body effects in two-dimensional crystals: Monolayer MoS_2, Phys. Rev. B **93**, 235435 (2016).

[12] N. Tancogne-Dejean, C. Giorgetti, and V. Véniard, Optical properties of surfaces with supercell *ab initio* calculations: Local-field effects, Phys. Rev. B **92**, 245308 (2015).

[13] L. Hedin, New method for calculating the one-particle Green's function with application to the electron-gas problem, Phys. Rev. **139**, A796 (1965).

[14] L. Hedin and S. Lundqvist, Effects of electron-electron and electron-phonon interactions on the one-electron states of solids, in *Solid State Physics, Advances in Research and Applications*, edited by F. Seitz, D. Turnbull, and H. Ehrenreich (Academic Press, New York, 1969), Vol. 23, pp. 1–181.

[15] G. Strinati, Application of the Green's functions method to the study of the optical properties of semiconductors, Riv. Nuovo Cimento **11**, 1 (1988).

[16] W. Hanke, Dielectric theory of elementary excitations in crystals, Adv. Phys. **27**, 287 (1978).

[17] W. Hanke and L. J. Sham, Many-particle effects in the optical spectrum of a semiconductor, Phys. Rev. B **21**, 4656 (1980).

[18] S. Albrecht, L. Reining, R. Del Sole, and G. Onida, *Ab initio* calculation of excitonic effects in the optical spectra of semiconductors, Phys. Rev. Lett. **80**, 4510 (1998).

[19] M. Rohlfing and S. G. Louie, Electron-hole excitations in semiconductors and insulators, Phys. Rev. Lett. **81**, 2312 (1998).

[20] L. X. Benedict, E. L. Shirley, and R. B. Bohn, Optical absorption of insulators and the electron-hole interaction: An *ab initio* calculation, Phys. Rev. Lett. **80**, 4514 (1998).

[21] G. Onida, L. Reining, and A. Rubio, Electronic excitations: Density-functional versus many-body Green's-function approaches, Rev. Mod. Phys. **74**, 601 (2002).

[22] T. Kotani, M. van Schilfgaarde, and S. V. Faleev, Quasiparticle self-consistent *GW* method: A basis for the independent-particle approximation, Phys. Rev. B **76**, 165106 (2007).

[23] D. Pashov, S. Acharya, W. R. Lambrecht, J. Jackson, K. D. Belashchenko, A. Chantis, F. Jamet, and M. van Schilfgaarde, QUESTAAL: A package of electronic structure methods based on the linear muffin-tin orbital technique, Comput. Phys. Commun., **249**, 107065 (2019).

[24] F. Aryasetiawan and O. Gunnarsson, Product-basis method for calculating dielectric matrices, Phys. Rev. B **49**, 16214 (1994).

[25] M. van Schilfgaarde, T. Kotani, and S. Faleev, Quasiparticle self-consistent *GW* Theory, Phys. Rev. Lett. **96**, 226402 (2006).

[26] C. Bhandari, M. van Schilfgaarde, T. Kotani, and W. R. L. Lambrecht, All-electron quasiparticle self-consistent *GW* band structures for $SrTiO_3$ including lattice polarization corrections in different phases, Phys. Rev. Mater. **2**, 013807 (2018).

[27] M. Shishkin, M. Marsman, and G. Kresse, Accurate quasiparticle spectra from self-consistent *GW* calculations with vertex corrections, Phys. Rev. Lett. **99**, 246403 (2007).

[28] W. Chen and A. Pasquarello, Accurate band gaps of extended systems via efficient vertex corrections in *GW*, Phys. Rev. B **92**, 041115(R) (2015).

[29] B. Cunningham, M. Grüning, P. Azarhoosh, D. Pashov, and M. van Schilfgaarde, Effect of ladder diagrams on optical absorption spectra in a quasiparticle self-consistent *GW* framework, Phys. Rev. Mater. **2**, 034603 (2018).

[30] B. Cunningham, M. Grüning, D. Pashov, and M. van Schilfgaarde, QS$G\hat{W}$: Quasiparticle self-consistent *GW* with ladder diagrams in *W*, Phys. Rev. B **108**, 165104 (2023).

[31] S. K. Radha, W. R. L. Lambrecht, B. Cunningham, M. Grüning, D. Pashov, and M. van Schilfgaarde, Optical response and band structure of $LiCoO_2$ including electron-hole interaction effects, Phys. Rev. B **104**, 115120 (2021).

[32] A. Jain, S. P. Ong, G. Hautier, W. Chen, W. D. Richards, S. Dacek, S. Cholia, D. Gunter, D. Skinner, G. Ceder, and K. A. Persson, Commentary: The materials project: A materials genome approach to accelerating materials innovation, APL Mater. **1**, 011002 (2013).

[33] Materials Project, mp-1023936, https://next-gen.materialsproject.org/materials/mp-1023936?formula=WSe2.

[34] H. Mishra, A. Bose, A. Dhar, and S. Bhattacharya, Exciton-phonon coupling and band-gap renormalization in monolayer WSe_2, Phys. Rev. B **98**, 045143 (2018).

[35] D. Deguchi, K. Sato, H. Kino, and T. Kotani, Accurate energy bands calculated by the hybrid quasiparticle self-consistent *GW* method implemented in the ecalj package, Jpn. J. Appl. Phys. **55**, 051201 (2016).

[36] T. Sander, E. Maggio, and G. Kresse, Beyond the Tamm-Dancoff approximation for extended systems using exact diagonalization, Phys. Rev. B **92**, 045209 (2015).

[37] T. Cheiwchanchamnangij and W. R. L. Lambrecht, Quasiparticle band structure calculation of monolayer, bilayer, and bulk MoS_2, Phys. Rev. B **85**, 205302 (2012).

[38] M. Marsili, A. Molina-Sánchez, M. Palummo, D. Sangalli, and A. Marini, Spinorial formulation of the *GW*-BSE equations and spin properties of excitons in two-dimensional transition metal dichalcogenides, Phys. Rev. B **103**, 155152 (2021).

[39] A. Ramasubramaniam, Large excitonic effects in monolayers of molybdenum and tungsten dichalcogenides, Phys. Rev. B **86**, 115409 (2012).

[40] D. Y. Qiu, F. H. da Jornada, and S. G. Louie, Optical spectrum of MoS_2: Many-body effects and diversity of exciton states, Phys. Rev. Lett. **111**, 216805 (2013).

[41] S.-Y. Chen, Z. Lu, T. Goldstein, J. Tong, A. Chaves, J. Kunstmann, L. S. R. Cavalcante, T. Woźniak, G. Seifert, D. R. Reichman, T. Taniguchi, K. Watanabe, D. Smirnov, and J. Yan, Luminescent emission of excited Rydberg excitons from monolayer WSe_2, Nano Lett. **19**, 2464 (2019).

[42] E. Liu, J. van Baren, T. Taniguchi, K. Watanabe, Y.-C. Chang, and C. H. Lui, Magnetophotoluminescence of exciton Rydberg states in monolayer WSe_2, Phys. Rev. B **99**, 205420 (2019).

[43] K. He, N. Kumar, L. Zhao, Z. Wang, K. F. Mak, H. Zhao, and J. Shan, Tightly bound excitons in monolayer WSe_2, Phys. Rev. Lett. **113**, 026803 (2014).

[44] A. V. Stier, N. P. Wilson, K. A. Velizhanin, J. Kono, X. Xu, and S. A. Crooker, Magneto-optics of exciton Rydberg states in a monolayer semiconductor, Phys. Rev. Lett. **120**, 057405 (2018).

[45] E. Liu, J. van Baren, Z. Lu, T. Taniguchi, K. Watanabe, D. Smirnov, Y.-C. Chang, and C. H. Lui, Exciton-polaron Rydberg states in monolayer $MoSe_2$ and WSe_2, Nat. Commun. **12**, 6131 (2021).

[46] T. Wang, Z. Li, Y. Li, Z. Lu, S. Miao, Z. Lian, Y. Meng, M. Blei, T. Taniguchi, K. Watanabe, S. Tongay, D. Smirnov, C. Zhang, and S.-F. Shi, Giant valley-polarized Rydberg excitons in monolayer WSe_2 revealed by magneto-photocurrent spectroscopy, Nano Lett. **20**, 7635 (2020).

[47] S. Y. Woo, A. Zobelli, R. Schneider, A. Arora, J. A. Preuß, B. J. Carey, S. Michaelis de Vasconcellos, M. Palummo, R. Bratschitsch, and L. H. G. Tizei, Excitonic absorption signatures of twisted bilayer WSe_2 by electron energy-loss spectroscopy, Phys. Rev. B **107**, 155429 (2023).

[48] A. Arora, M. Koperski, K. Nogajewski, J. Marcus, C. Faugeras, and M. Potemski, Excitonic resonances in thin films of WSe_2: from monolayer to bulk material, Nanoscale **7**, 10421 (2015).

[49] R. Schmidt, I. Niehues, R. Schneider, M. Drüppel, T. Deilmann, M. Rohlfing, S. M. de Vasconcellos, A. Castellanos-Gomez, and R. Bratschitsch, Reversible uniaxial strain tuning in atomically thin WSe_2, 2D Mater. **3**, 021011 (2016).

[50] G. Wang, X. Marie, I. Gerber, T. Amand, D. Lagarde, L. Bouet, M. Vidal, A. Balocchi, and B. Urbaszek, Giant enhancement of the optical second-harmonic emission of WSe_2 monolayers by laser excitation at exciton resonances, Phys. Rev. Lett. **114**, 097403 (2015).

[51] Y. Li, A. Chernikov, X. Zhang, A. Rigosi, H. M. Hill, A. M. van der Zande, D. A. Chenet, E.-M. Shih, J. Hone, and T. F.

Heinz, Measurement of the optical dielectric function of monolayer transition-metal dichalcogenides: MoS_2, $MoSe_2$, WS_2, and WSe_2, Phys. Rev. B **90**, 205422 (2014).

[52] J. Wierzbowski, J. Klein, F. Sigger, C. Straubinger, M. Kremser, T. Taniguchi, K. Watanabe, U. Wurstbauer, A. W. Holleitner, M. Kaniber, K. Müller, and J. J. Finley, Direct exciton emission from atomically thin transition metal dichalcogenide heterostructures near the lifetime limit, Sci. Rep. **7**, 12383 (2017).

[53] J. Madéo, M. K. L. Man, C. Sahoo, M. Campbell, V. Pareek, E. L. Wong, A. Al-Mahboob, N. S. Chan, A. Karmakar, B. M. K. Mariserla, X. Li, T. F. Heinz, T. Cao, and K. M. Dani, Directly visualizing the momentum-forbidden dark excitons and their dynamics in atomically thin semiconductors, Science **370**, 1199 (2020).

[54] J. Li, M. Goryca, N. P. Wilson, A. V. Stier, X. Xu, and S. A. Crooker, Spontaneous valley polarization of interacting carriers in a monolayer semiconductor, Phys. Rev. Lett. **125**, 147602 (2020).

[55] T. Deilmann and K. S. Thygesen, Dark excitations in monolayer transition metal dichalcogenides, Phys. Rev. B **96**, 201113(R) (2017).

[56] M. Rohlfing, Electronic excitations from a perturbative LDA + *GdW* approach, Phys. Rev. B **82**, 205127 (2010).

[57] T. Deilmann and K. S. Thygesen, Finite-momentum exciton landscape in mono- and bilayer transition metal dichalcogenides, 2D Mater. **6**, 035003 (2019).

[58] Y. Song and H. Dery, Transport theory of monolayer transition-metal dichalcogenides through symmetry, Phys. Rev. Lett. **111**, 026601 (2013).

[59] O. Atabek, C. Deutsch, and M. Lavaud, Schrödinger equation for the two-dimensional Coulomb potential, Phys. Rev. A **9**, 2617 (1974).

[60] https://github.com/Electronic-Structure-Group/wse2-excitons.